Synthesis of minerals

Bublikova T.M., Setkova T.V., Balitsky V.S., Nekrasov A.N., Drozhzhina N.A. Synthesis of fine-crystalline malachite and its application to increase wear resistance of natural mineral samples. *UDC 553.897.431.2:549.07*

D.S. Korzhinskii Institute of Experimental Mineralogy RAS, Chernogolovka tmb@iem.ac.ru

Abstract. Experiments on growing a layer of synthetic malachite on surface of natural malachite were carried out in recirculation-type crystallizers using solutions of ammonia hydroxide. It has been established that the crystallization of malachite in low concentrated solutions (0.2–0.5 m NH_4OH) occurs at low crystal growth rates (10–13 μm/day). A characteristic feature of synthetic malachite is the high density of crystals, the absence of macrovoids and free cavities with inclusions of the crystallization solution. The established presence of hardness anisotropy of the second kind in synthetic malachite suggests the possibility of using fine-crystalline synthetic malachite to increase the wear resistance of natural malachite during the renewal and restoration of rare samples and products made from natural malachite.

***Keywords**: synthetic fine crystalline malachite, ammonium hydroxide, recirculation crystallizer, hardness anisotropy, scanning electron microscopy*

The developed methods for obtaining a synthetic analogue of malachite have opened up new prospects for its use. Research by Russian art historians has shown the possibility of using high-quality synthetic malachite for renewal, restoration and replacement of damaged fragments of unique museum specimens (Shuisky, 2015). Natural and synthetic malachite is widely used as a jewelry stone, despite a number of inherent disadvantages. The relatively low hardness of malachite (3.5–4.0 on the Mohs scale) is the reason abrasion of the polished surface of the mineral. Malachite is sensitive to even mildly aggressive environments (Budrina, 2020; Mukendi, 2009; Chernenko, Melnikov, 2003; Petrov et al., 2013).

Under natural conditions, the deposition of malachite from solution often occurs along cracks, in voids of various shapes in carbonate rocks. Crystals in the growing layer are located in different directions, which is especially pronounced in malachite with a concentric-zonal structure (Fig. 1a). In the diverse morphological types of malachite, fluctuations in hardness indicators are noted. We have measured the microhardness of malachite depending on the arrangement of crystals in malachite aggregates of different origins. The measurements were carried out on a PMT-3 device with a load of 50 g (PMT-3 microhardness tester). 17 samples of natural (10) and synthetic (7) malachite were studied (more than 200 measurements). The results obtained showed the absence of a significant difference in the hardness of natural and synthetic malachite (Table 1). However, the spread of microhardness values indicates an anisotropy of hardness of the second kind (k ~ 1.1). It has been established that crystal faces perpendicular to the growth direction have higher hardness than faces parallel to the crystallization front.

Previous studies of the conditions of formation and morphology of synthetic malachite showed that changing the crystallization parameters of the mineral makes it possible to obtain its different textural types. In a number of experiments, we obtained fine-crystalline malachite with crystal sizes of 200–1000 nm and 3–7 μm (in transverse size) (Bublikova et al. 2019, 2022). We have established the presence of anisotropy in the hardness of malachite of the second kind. Growing a layer of fine-crystalline malachite (Fig. 1b, zone 1) perpendicular to the crystallization front on the surface of natural malachite (Fig. 1b, zone 2) can presumably increase its hardness and wear resistance.

Table 1. Microhardness of faces perpendicular and parallel to the direction of crystal growth in samples of natural and synthetic malachite

Genesis	Mohs hardness	Hardness of the malachite sample face along the direction of crystal growth, kg/mm^2	Hardness of the face of a malachite sample perpendicular to the growth direction, kg/mm^2	Deviation, %
Chokpak deposit (Kazakhstan)	4.0–4.5	256.5	282.9	10.4
Kolwezi deposit (DR Congo)	4.0–4.5	257.1	289.1	11.1
Synthetic malachite (IEM RAS)	4.0–4.5	263.6	279.9	6.9

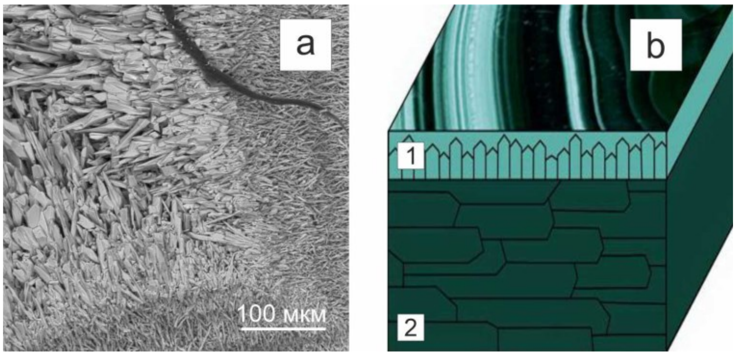

Fig. 1. a – SEM image of crystals in differently colored zones of a sample of natural malachite (DR Congo); b – schematic representation of the arrangement of crystals in a sample of natural (2) and synthetic (1) malachite

Experiments on growing a layer of fine-crystalline malachite on natural samples were carried out in recirculation-type crystallizers. Their design was developed at the IEM RAS (Bublikova et al., 2000). Polished plates of natural malachite from the Kolwezi deposit (DR Congo) were used as samples. Ammonium hydroxide with a concentration of 0.2–2.5 m NH_4OH was used as working solutions. The crystallization temperature was maintained at 75 ± 1 °C to obtain the most homogeneous layer possible.

Since malachite has high solubility in ammonia solutions, their effect on the surface layer of malachite was previously studied. It has been established that in weakly concentrated solutions, etching grooves with a depth of up to 100 µm appear on the surface of the samples already in the first 2–5 hours. In stronger solutions, a copper hydroxide phase is additionally formed. Since the process of malachite synthesis includes successive stages of dissolution of the charge, saturation of the solution volume with copper and carbon dioxide, crystallization of malachite begins a few days after the experiment. The surface of natural malachite samples placed in a crystallizer is damaged by the ammonia solution. Thus, in order to maximize the preservation of the polished surface, it is advisable to carry out experiments on the crystallization of a new layer on malachite samples in two stages.

At the first stage, the charge material, basic copper carbonate, was loaded into the crystallizer, an ammonia solution was poured in, and kept in the specified mode for 25–30 days. Then the crystallizer was opened and samples of natural malachite were placed in it. In total, the duration of the experiments was 50–60 days.

In all experiments, the resulting growth was represented by dense crystalline malachite. The internal structure of malachite samples was studied on chipped and polished surfaces using a Tescan Vega II XMU raster scanning microscope.

In the malachite buildup obtained in experiments using concentrated solutions of 2.0–2.5 m NH_4OH, there are microcracks and voids filled with the solution. The crystal sizes are close to those of natural Zairean malachite crystals (15–20 µm in transverse size). The best results were obtained in experiments where a solution of 0.5 m NH_4OH was used (Fig. 2c). The thickness of the layer of synthetic malachite was 80–150 µm (Fig. 2a). The crystals are located perpendicular to the surface of the natural malachite sample (Fig. 2b). The overgrown layer is represented by fine-crystalline malachite with a high density of crystals. Malachite aggregates consist of elongated prismatic crystals measuring 4–8 µm in transverse size, the crystals are arranged in parallel.

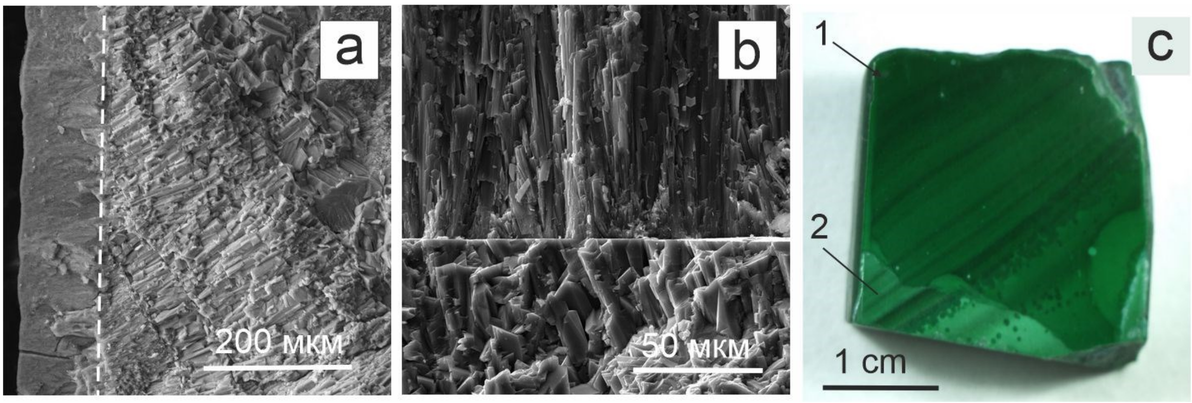

Fig. 2. a, b – SEM images and c – photograph of a sample of natural malachite (2) with an overgrown layer of synthetic fine-crystalline malachite (1)

Crystallization of malachite in weakly concentrated solutions (0.2–0.5 m NH_4OH) occurs at low crystal growth rates (10–13 µm/day). Synthesized malachite does not contain macrovoids, free cavities filled with solution. This malachite is less porous than malachite obtained in highly concentrated solutions. The thickness of the layer of fine-crystalline malachite after polishing was 30–50 µm. The layer is transparent. The texture pattern of the natural sample is preserved. Microhardness measurements of the built-up layer showed that they correspond to the maximum for malachite 290–320 kg/mm^2.

Thus, the developed method made it possible to obtain a build-up of synthetic malachite of high hardness on the surface of natural samples. The use of this method can be promising in the restoration, renewal, and replacement of damaged fragments of products and rare museum samples of malachite.

This study is fulfilled under Research program № FMUF-2022-0002 of the Korzhinskii Institute of Experimental Mineralogy

References

Bublikova T.M., Balitsky V.S., Timokhina I.V. Synthesis and main properties of jewelry and orrnametal malachite. Synthesis of minerals. V. 1. Alexandrov, VNIISIMS. 2000. 662 p. (In Russian).

Bublikova T.M., Balitsky V.S., Nekrasov A.N., Setkova T.V., Krikunova P.V., Mikhailova P.S., Gavrilova E.O. Experimental investigation of the influence of the concentration of ammonia solutions on the sizes of malachite crystals in the mass crystallization process. Experiment in GeoSciences, 28(1):127–129, 2022.

Budrina L.A. Malachite diplomacy. Moscow; Ekaterinburg: Armchair scientist. 2020. 208 p.

Mukendi E.B. Criteria of the geological–commercial assessment of malachite from the Democratic Republic of the Congo, Cand. Sci, (Geol.-Min.) Dissertation, Moscow: Mosk. Geol.-Razved. Inst., 2009.

Chernenko T.V. and Melnikov E.P., Properties and diagnostics of natural and synthetic malachite, Vestn. Gemmol., 2003, N 8–9, pp. 11–26.

Petrov T.G., Protopopov E.N., Shuyskiy A.V. Decorative grown malachite. Nature and technology // Russian Journale of Earth Sciences. 2013. Vol. 13. № 2.

Shuyskiy, A.V., Experimental mineralogy and genesis of synthetic malachite, Cand. Sci. (Geol.-Min.) Dissertation, St. Petersburg: St. Petersburg Gos. Univ., 2015.

Kotelnikov A.R.[1], Suk N.I.[1], Akhmedzhanova G.M.[1], Kotelnikova Z.A.[2], Drozhzhina N.A.[1]

Study of cation exchange equilibria of (K,Rb)-gallium feldspars. *UDC 550.89:549.07*

[1]IEM RAS, Chernogolovka, Moscow region; [2]IGEM RAS, Moscow (kotelnik1950@yandex.ru)

Abstract. Gallium-containing feldspars $KGaSi_3O_8$ and $RbGaSi_3O_8$ were synthesized by hydrothermal crystallization at 550℃ and a pressure of 1.5 kbar. Their unit cell parameters have been refined. Cation exchange equilibria of potassium-rubidium gallium-containing feldspars with a 1 M KCl + RbCl solution at 550℃ and a pressure of 1.5 kbar were studied. Based on the experimental data, the unit cell parameters of the $(K,Rb)GaSi_3O_8$ solid solution was calculated. Based on the distribution coefficients of K, Rb in the feldspar – solution system, the excess mixing energies were calculated. According to the calculation results, the $(K,Rb)GaSi_3O_8$ solid solution is close to ideal.

Keywords*: feldspars, synthesis, unit cell parameters, solid solutions, experiment*

Introduction. Gallium alkali feldspars of the $KGaSi_3O_8$ – $RbGaSi_3O_8$ series are interesting for studying the properties of minerals of the group of framework aluminosilicates, as well as as models of solid solutions in which structural ordering largely determines their thermodynamic properties. On the other hand, studying the features of the inclusion of rubidium and gallium in solid solutions of feldspars is of undoubted interest for the geochemistry of rare elements of the earth's crust.

The synthesis of gallium- and germanium-containing feldspars was first described in the work of Goldsmith (1950); subsequently, many researchers studied such feldspars; a review of these works is given in the work of H.U. Bambauer et al. (1974) and in the monograph of H. Pentinghaus (1980). The synthesis of the gallium analogue of sanidine is described in the work of M. Kimata et al. (1995). No one has yet carried out the synthesis of $RbGaSi_3O_8$. Thus, the purpose of this work was the synthesis and X-ray study of gallium feldspars $RbGaSi_3O_8$ and $RbGaSi_3O_8$, and the study of their properties. In addition, using the method of cation exchange reactions, we had to synthesize and study solid solutions of potassium-rubidium gallium-containing feldspars.

Experimental results

Gallium-containing feldspars $KGaSi_3O_8$ and $RbGaSi_3O_8$ were synthesized by hydrothermal crystallization at 550°C and a pressure of 1.5 kbar. Gallium feldspars have been studied by microprobe and X-ray analysis.

To calculate the parameters, 61 reflections were used (81% of all) - for $RbGaSi_3O_8$; and 64 reflections (90%) for $KGaSi_3O_8$. The parameters were refined for the space group c2/m. The unit cell parameters values for the endmembers of the solid solution are as follows. For $RbGaSi_3O_8$:

a=8.903(1)[A]; b=13.095(1)[A]; c= 7.228(1)[A]; β =116.39(1)[°]; V= 754.9(2) [A^3];

for $KGaSi_3O_8$: a=8.654(1)[A]; b=13.076(2)[A];

c=7.221(1) [A]; β = 116.08(1) [°]; V = 733.9(2)[A^3].

Experiments on cation exchange of (K,Rb)$GaSi_3O_8$ solid solutions with water-salt fluid (H_2O + 1M KCl + 1M RbCl) were carried out at a temperature of 550℃ and P = 1.5 kbar, the experimental results are given in Table 1.

Figure 1 shows the distribution isotherm of potassium and rubidium between (K,Rb)$GaSi_3O_8$ feldspars and aqueous-salt fluid. The compositions of the coexisting phases are given in mole fractions (X_{Rb}^{Fsp} and X_{Rb}^{fl}). It can be seen that at compositions X_{Rb}^{Fsp} = 0 – 0.64, rubidium enriches the fluid relative to feldspar. At X_{Rb}^{Fsp} values > 0.65, rubidium is redistributed predominantly into feldspar (relative to the fluid). The dependence of ln(KD) on the composition of the solid solution is described by the linear equation:

$\ln(K_D) = -0.632 + 0.768 * X_{Rb}^{Fsp}$; n=8; r=0.78; E_x = 0.14.

Table 1. Compositions of equilibrium solid solutions of (K,Rb)$GaSi_3O_8$ and fluids at 550^{o}C and P=1.5 kbar.

N run.	X_{Rb}^{Fsp} п/о	X_{Rb}^{fl} п/о	K_D	$\ln(K_D)$
7494	0.083	0.156	0.490	-0.713
7491	0.108	0.195	0.500	-0.693
7535	0.256	0.299	0.810	-0.211
7493	0.405	0.514	0.640	-0.446
7532	0.420	0.440	0.920	-0.083
7536	0.614	0.658	0.830	-0.186
7549	0.796	0.824	0.833	-0.183
7548	0.846	0.849	0.977	-0.023

Table 2. Unit cell parameters of the solid solution of (K,Rb)$GaSi_3O_8$

N run.	X_{Rb}^{Fsp}	a, [A]	b, [A]	c, [A]	β, [°]	V, [A^3]	n
7540	0.000	8.654	13.076	7.221	116.080	733.900	56
7494	0.083	8.671	13.080	7.218	116.120	735.000	57
7491	0.108	8.677	13.076	7.221	116.140	735.500	53
7535	0.256	8.716	13.079	7.226	116.160	739.400	59
7544	0.346	8.731	13.082	7.231	116.190	741.200	59
7493	0.406	8.764	13.082	7.226	116.180	743.500	41
7532	0.420	8.765	13.083	7.231	116.190	744.100	62
7533	0.551	8.805	13.083	7.227	116.220	746.900	49
7534	0.598	8.821	13.084	7.231	116.260	748.500	53
7536	0.614	8.827	13.088	7.230	116.250	749.100	55
7549	0.796	8.871	13.092	7.226	116.290	752.400	62
7548	0.846	8.883	13.091	7.227	116.320	753.400	51
7541	1.000	8.903	13.095	7.228	116.390	754.900	65

The unit cell parameters of the synthesized potassium-rubidium gallium feldspars were calculated using an internal standard (silicon), and reflection correction was performed using the polygonal method. The unit cell parameters values of the synthesized feldspars are shown in Fig. 2(a, b) and in Table 2.

Based on the data in Table 2, the concentration dependences of unit cell parameters on the composition of the solid solution were calculated:

$a = 8.6540 + 0.154714*x + 0.371795*x^2 - 0.277907*x^3$; [A], ($E_x$ = 0.001)

$b = 13.076 + 0.010617*x + 0.0110097*x^2 - 0.002778*x^3$; [A], ($E_x$ = 0.001)

$c = 7.220 + 0.036081*x - 0.0460276*x^2 + 0.021714*x^3$; [A], ($E_x$ = 0.001)

$\beta = 116.08 + 0.403292*x - 0.430358*x^2 + 0.334396*x^3$; [°], ($E_x$ = 0.005)

$V = 733.80 + 15.1666*x + 29.4337*x^2 - 23.5592*x^3$; [A^3], ($E_x$ = 0.10),

where x – mole fraction of rubidium in solid solution (K,Rb)$GaSi_3O_8$.

Processing of experimental results

Calculation of excess mixing volumes of solid solutions of potassium-rubidium gallium feldspars. As the initial data for the calculation, we used the unit cell parameters calculated for the synthesized gallium feldspars (Table 2). The calculation was performed according to the dependence: $V^{ex} = V - V^{id}$; used the following equation:

$V^{ex} = [(733.80+15.1666*x + 29.4337*x^2 - 23.5592*x^3)-(733.8+21.06*x)]/6.6408$ (cm^3/mol), where x – mole fraction of rubidium in (K,Rb)-gallium feldspar.

The excess volume of mixing has an alternating character: at $X_{Rb}^{Fsp} < 0.2$ the volume is negative, at $X_{Rb}^{Fsp} > 0.25$ it is positive. The obtained values of excess mixing volumes are well described by the following polynomial of the 3rd degree:

$V^{ex} = 0.000048 - 0.799686*x + 4.227723*x^2 - 3.4279506*x^3$.

Using the least squares method, the values of the parameters of the Margules model were calculated from this polynomial: W1=2.63(1) и W2=-0.87(1) cm^3/mol.

Calculation of excess mixing energies of solid solutions of potassium-rubidium gallium feldspars. From the experimental data we obtained based on the results of studying the cation exchange equilibria of (K,Rb)GaSi$_3$O$_8$ and fluid, we can calculate the excess mixing energies of the solid solution. The excess mixing energy is described within the framework of the symmetric Margules model: W1=W2=2.62(2) kJ/mol.

Conclusions

1. Gallium-containing feldspars KGaSi$_3$O$_8$ and RbGaSi$_3$O$_8$ were synthesized by hydrothermal crystallization at 550°C and a pressure of 1.5 kbar. Their unit cell parameters have been refined.

2. Cation exchange equilibria of potassium-rubidium gallium-containing feldspars with a 1M KCl+RbCl solution at 550°C and a pressure of 1.5 kbar were studied.

3. Based on experimental data, the excess mixing functions of the (K,Rb)GaSi$_3$O$_8$ solid solution were calculated.

The work was supported by the FMUF-2022-0002 program.

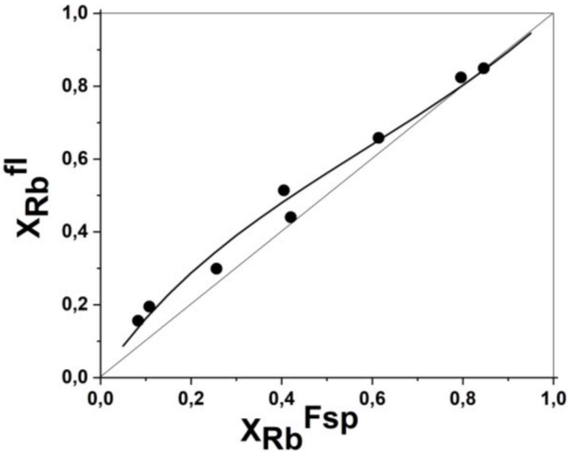

Fig. 1. Isotherm of distribution of potassium and rubidium between feldspars (K,Rb)GaSi$_3$O$_8$ and water-salt fluid at 550°C and P=1.5 kbar**.**

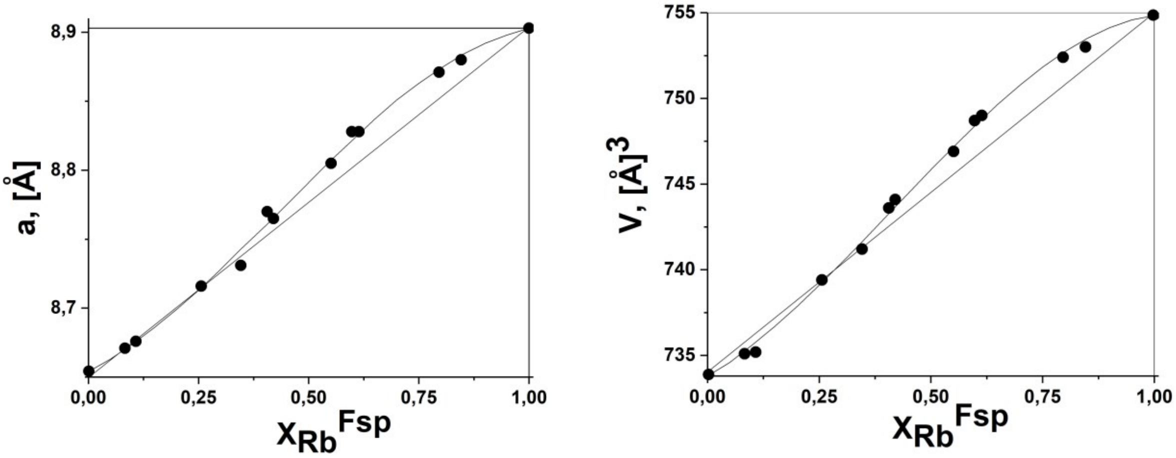

Fig. 2. Dependences of the unit cell parameters of the (K,Rb)GaSi$_3$O$_8$ solid solution on the composition.

References

1. Bambauer H.U., Kroll H., Nager H.E., Pentinghaus H. Feldspat–Mischkristalle – Eine Ubersicht. Bull. Soc. fr. Mineral. Cristallogr., 1974, V.97, P.313-345.
2. Pentinghaus H. Polimorphie in den feldspatbildenden systemen A+T3+T4+O8 und A2+T23+T24+O8 alkali- und erdalkali-, bor-, aluminium-, gallium-, eisen-silicate und –germanate. Habil. Diss. Munster. 1980. 210 p.
3. Kimata M., Saito S., Shimizu M. Structure of sanidine type $KGASi_3O_8$ tetrahedral-site disordering in potassium feldspar. Eur. J. Mineral., 1995, V.7. P. 287-296.

Kotelnikov A.R., Suk N.I., Akhmedzhanova G.M., Drozhzhina N.A. Synthesis of (Rb,Ba)-feldspar solid solutions. *UDC 550.89:549.07*

IEM RAS, Chernogolovka, Moscow region
kotelnik1950@yandex.ru

Abstract. Rubidium feldspar was synthesized from glass with the composition $RbAlSi_3O_8$ by hydrothermal recrystallization at 650℃ and a pressure of 2 kbar. Barium feldspar ($BaAl_2Si_2O_8$) is prepared by pyrosynthesis from a mixture of silicon and aluminum oxides and barium carbonate at 1340℃. Using the method of cation exchange reactions: $2RbAlSi_3O_8 + BaCl_{2(aq)} = BaAl_2Si_2O_8 + 4SiO_2 + 2RbCl_{(aq)}$ at 650℃ and a pressure of 2 kbar, solid solutions of rubidium-barium feldspars were synthesized. The compositions of solid solutions were determined by microprobe analysis. An X-ray study of the synthesized feldspars was carried out, and the parameters of the unit cells were refined. The concentration dependences of the unit cell parameters were plotted. Excess volumes of mixing of (Rb,Ba)-feldspar solid solutions are calculated. They are described quite well by the two-parameter Margules model.

Keywords: *solid solutions, synthesis, rubidium, barium, experiment*

Rubidium feldspar was synthesized from glass with the composition $RbAlSi_3O_8$ by hydrothermal recrystallization at 650°C and a pressure of 2 kbar. Barium feldspar ($BaAl_2Si_2O_8$) was prepared by pyrosynthesis from a mixture of silicon and aluminum oxides and barium carbonate. The synthesis temperature was 1340°C, duration 20 hours. After annealing, the sample was ground and recrystallized at 850°C and a pressure of 3.5 kbar in a 1 M $BaCl_2$ solution. Synthetic feldspars (Fig. 1) were studied by X-ray analysis, and their unit cell parameters (UCP) were refined.

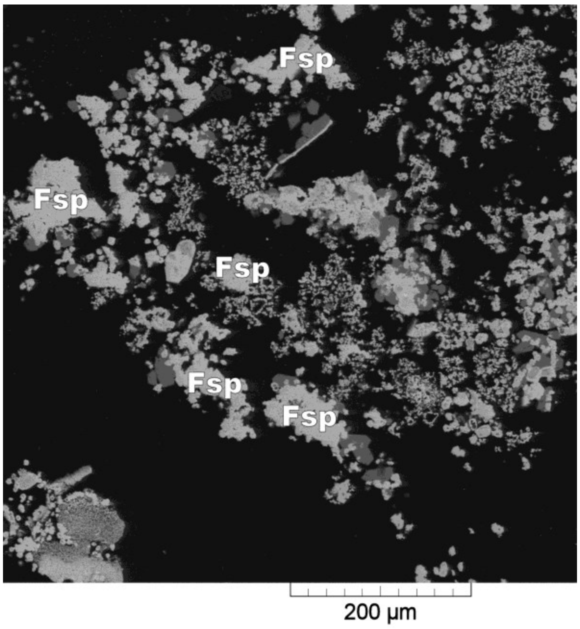

Fig. 1. Synthesized Rb,Ba-feldspars (Fsp). Sample 7550.

By cation exchange reaction method: $2RbAlSi_3O_8 + BaCl_{2(aq)} = BaAl_2Si_2O_8 + 4SiO_2 + 2RbCl_{(aq)}$ solid solutions of rubidium-barium feldspars were synthesized at 650°C and a pressure of 2 kbar. The compositions of solid solutions were determined by microprobe analysis. An X-ray study of the synthesized feldspars was carried out, and the parameters of the unit cells were refined. Data on the unit cells parameters are presented in Table 1 and Fig. 2 (a, b, c). Using the method of data approximation by polynomials of the 3rd degree, equations for the dependence of the UCP on the composition of rubidium-barium feldspars were obtained:

$a = 8.839 - 0.388136*x + 0.221442*x^2 - 0.0408732*x^3$ [A];
$R^2 = 0.999$; Ex=0.001
$b = 13.018 + 0.029799*x + 0.058204*x^2 - 0.0712217*x^3$ [A];
$R^2 = 0.921$; Ex=0.001
$c = 7.186 + 0.0035519*x + 0.0777873*x^2 - 0.071573*x^3$ [A];
$R^2 = 0.980$; Ex=0.0005
$\beta = 116.314 - 1.297408*x + 2.55251*x^2 - 2.437878*x^3$ [°];
$R^2 = 0.999$; Ex=0.006
$V = 741.1 - 19.4087*x + 7.0419*x^2 + 4.209842*x^3$ [A^3];
$R^2 = 0.997$; Ex=0.09,

X – mole fraction of barium in solid solution of feldspars.

Excess volumes of mixing solid solutions (Rb,Ba)-feldspars are calculated. They are described quite well by the two-parameter Margules model: W1 = -2.42(2) cm^3/mol and W2 = -1.90(3) cm^3/mol. The excess volume of mixing is negative throughout the entire range of compositions.

The work was supported by the FMUF-2022-0002 program.

Table 1. Parameters of unit cells of Rb,Ba-feldspars

№ sample	X_{Ba}^{Fsp}	a, [Å]	b, [Å]	c, [Å]	β, [°]	V, [Å]^3	n**
7539	0,000	8,839(1)	13,018(1)	7,186(1)	116,31(1)	741,1(2)	63
7529	0,041(21)	8,827(2)	13,020(1)	7,188(1)	116,27(1)	740,7(3)	61
7526	0,139(13)	8,787(2)	13,030(1)	7,188(1)	116,19(1)	738,6(3)	59
7552	0,161(26)	8,781(1)	13,031(1)	7,188(1)	116,15(1)	738,3(3)	52
7513	0,167(33)	8,782(1)	13,021(1)	7,189(1)	116,16(1)	738,5(4)	42
7512	0,168(21)	8,780(1)	13,026(2)	7,189(1)	116,19(1)	737,7(3)	54
7527	0,186(32)	8,774(1)	13,025(2)	7,189(1)	116,16(1)	738,0(3)	54
7551	0,191(45)	8,774(2)	13,029(1)	7,190(1)	116,13(1)	738,0(3)	41
7516	0,204(21)	8,772(1)	13,026(2)	7,188(1)	116,13(1)	737,6(3)	43
7515	0,210(22)	8,766(2)	13,025(2)	7,191(2)	116,16(1)	737,2(3)	50
7517	0,218(31)	8,767(2)	13,026(1)	7,191(1)	116,10(1)	737,3(4)	45
7550	0,285(55)	8,744(1)	13,032(1)	7,191(1)	116,07(1)	736,1(2)	57
7481	0,340(22)	8,727(2)	13,030(2)	7,193(1)	116,06(1)	735,4(4)	40
7480	0,567(31)	8,688(1)	13,038(1)	7,200(1)	115,95(1)	733,3(3)	40
7528	0,799(21)	8,647(3)	13,047(1)	7,203(2)	115,98(1)	732,7(4)	51
7538	1,000	8,632(1)	13,035(1)	7,196(1)	115,13(1)	733,0(2)	94

* measurement errors are given in parentheses and refer to the last decimal places; ** number of reflections used to calculate the unit cell parameters.

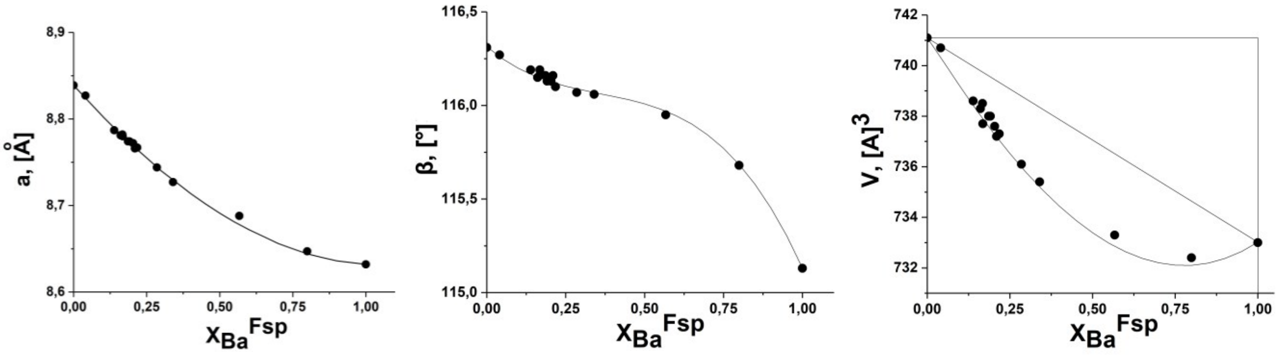

a b c

Fig. 2. Dependences of unit cell parameters on the composition of the solid solution: a – parameter a, [Å]; b – angle β [°]; c – cell volume [Å^3].

Kovalskaya T.N.[1], Ermolaeva V.N.[1,2], Kovalskiy G.A.[1], Varlamov D.A.[1,3], Chukanov N.V.[3], Chaychuk K.D.[1] Synthesis of zirconosilicates under high alkalinity conditions

[1] – IEM RAS, Chernogolovka; [2] – GEOKHI RAS, Moscow; [3] – FRC PCP MC RAS, Chernogolovka
tatiana76@iem.ac.ru

Abstract. Synthesis of zirconosilicates was carried out under of high alkalinity conditions at temperature 600°C and pressure of 2 kbar. According to the data of electron-probe microanalysis, X-ray diffraction and IR spectroscopy, minerals of eudialyte group, zirsinalite, parakeldyshite and aegirine were diagnosed in the synthesis products.

Keywords: *synthesis, zirconosilicates, eudialyte group minerals, zirsinalite, parakeldyshite.*

Zirconosilicates are widely distributed in alkaline massifs. A typical example is eudialyte group minerals, typical accessory minerals of the Lovozero alkaline massif, which are rock-forming minerals in eudialyte lujavrites of the massif. Minerals of the eudialyte group are concentrators of a number of rare elements (Zr, Hf, Nb, REE), and for this reason are of interest as a potential source of these elements. Idealized formula of eudialyte group minerals (Z=3, see Johnsen et al., 2003): $N1_3N2_3N3_3N4_3N5_3M1_6M2_{3\text{-}6}M3M4Z_3(Si_{24}O_{72})O'_{4\text{-}6}X1X2$, where N1-5 = Na, K, H_3O^+, Ca, Mn^{2+}, Sr, Ba, REE; M1 = Ca, Mn^{2+}, Fe^{2+}, REE, Na, Sr; M2 = Mn^{2+}, Fe^{2+}, Fe^{3+}, Na, Zr, Ta, Ti, K, H_3O^+; M3 and M4 = Si, S, Nb, Ti, W, Na; Z = Zr, Ti, Nb; O' = O, OH, H_2O; X1 and X2 = F, Cl, H_2O, OH, CO_3, SO_4. The minerals of the eudialyte group include 31 mineral species. Of these, 18 minerals were discovered in alkaline rocks of 3 large alkaline massifs of the Kola Peninsula (Khibiny, Lovozero, and Kovdor), and most of the minerals of the eudialyte group were identified here as accessory minerals of pegmatites. Earlier eudialyte was synthesized as a component of a polymineral association including aegirine, vlasovite and other zirconosilicates (Christophe-Michel-Lévy, 1961); in the present work eudialyte was identified from X-ray data.

The authors of the present work in order to reconstruct the physico-chemical conditions of formation of the typomorphic mineral of ultraalkaline complexes, eudialyte, several experiments on its synthesis were carried out and its identification was carried out by electron-probe microanalysis, X-ray diffraction and IR spectroscopy (Kovalskaya et. al., 2022; Kovalskaya et. al., 2022; Kovalskaya et. al., 2023). Further experiments showed that with increasing alkalinity of the solutions, more alkaline zirconosilicates, also characteristic of pegmatites of ultraalkaline complexes, are synthesized. In this work, in order to study the influence of solutions on the growth of zirconosilicates, experiments on their synthesis were carried out. Sol-gels of simplified eudialyte composition prepared by the gel technique were used as a starting mixture (Table 1). 1M NaCl solution and 46% NaOH solution were used as a fluid. For 100 mg of the initial mixture, 32 µl of 1M NaCl and 68 µl of 46% NaOH were taken. In 2 experiments, natural eudialyte (Northern part of Umbozero mine, Lovozero massif) was added to the initial mixture as an seed in the amount of 1% of the weight of the suspension, 2 experiments were conducted without inoculum. The experiments were carried out in a high-pressure gas reactors at a temperature of 600°C and a pressure of 2 kbar. The duration of the experiments was 10 days.

According to the data of electron-probe microanalysis (Fig. 1, Table 2), in the products of three experiments out of four, in addition to the newly formed mineral of eudialyte group (EGM), which differs in composition from the initial seed, the mineral of lovoserite group (zirsinalite), parakeldyshite and aegirine were also diagnosed. In addition, the presence of EGM, zirsinalite, parakeldyshite and aegirine was also confirmed by X-ray and IR spectroscopy.

Table 1. Composition of the starting mixture.

Component	weight (g) (routes 55-56)	weight (g) (routes 57-58)
SiO_2	0.90	0.76
$ZrOCl_2$	0.32	0.49
Nb_2O_5	0	0.07
Fe_2O_3	0.14	0.11
CaO	0.19	0.17
Na_2CO_3	0.45	0.40
Total	2.0	2.0

According to the data of electron-probe microanalysis, the newly formed eudialyte is characterized by a reduced iron content, and in one of the experiments (57), conducted without the use of seed, raslakite - EGM with increased zirconium content and reduced calcium content compared to natural eudialyte was formed (Table 2).

Table 2. Chemical composition of synthesized zirconosilicates.

Compo-nent	Route 55		Route 56		Route 57	Route 58		
	zirsinalite	parakeldy-shite	zirsinalite	parakeldy-shite	EGM	zirsinalite	parakeldy-shite	EGM
weight %								
Na_2O	26.74	18.60	27.47	21.74	15.74	27.54	19.30	19.06
CaO	7.49	0.45	5.51	2.98	5.87	10.72	2.58	13.05
FeO	bdl	bdl	bdl	bdl	6.79	bdl	bdl	0.94
ZrO_2	14.40	41.40	15.17	34.06	17.71	9.30	39.38	10.59
SiO_2	51.66	38.46	50.40	40.53	52.75	49.55	34.49	54.11
Nb_2O_5	bdl	bdl	bdl	bdl	0.72	1.54	2.25	0.99
Total	100.28	98.91	98.56	99.30	99.57	98.64	98.00	98.74
formulae coefficients								
Na	6.02	1.88	6.34	2.08	14.95	6.47	2.17	17.60
Ca	0.93	0.03	0.70	0.16	3.08	1.39	0.16	6.67
Fe	0	0	0	0	2.78	0	0	0.37
Zr	0.82	1.05	0.88	0.82	4.23	0.55	1.11	2.46
Si	6.00	2.00	6.00	2.00	25.83	6.00	2.00	25.78
Nb	0	0	0	0	0.17	0.09	0.06	0.22
Basis of calcula-tion	Si=6	Si=2	Si=6	Si=2	(Si+Nb)=26	Si=6	Si=2	(Si+Nb)=26

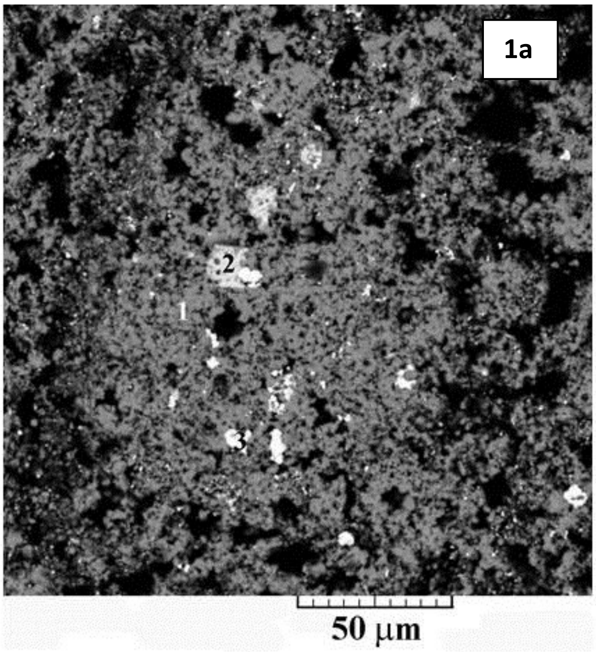

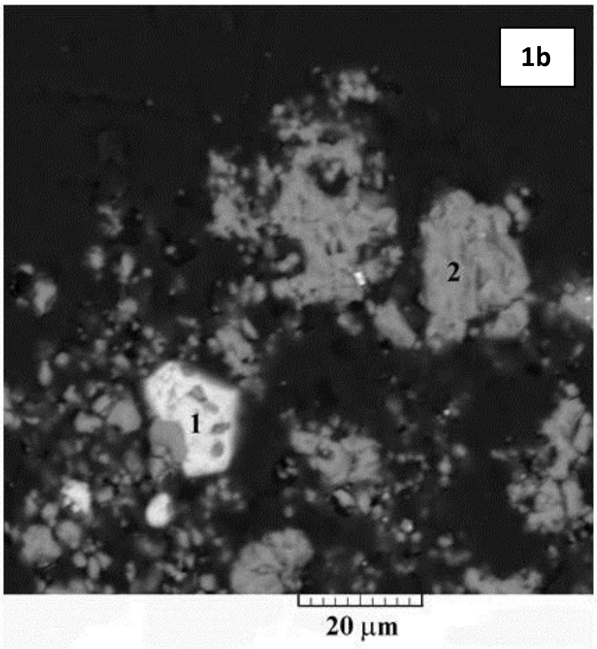

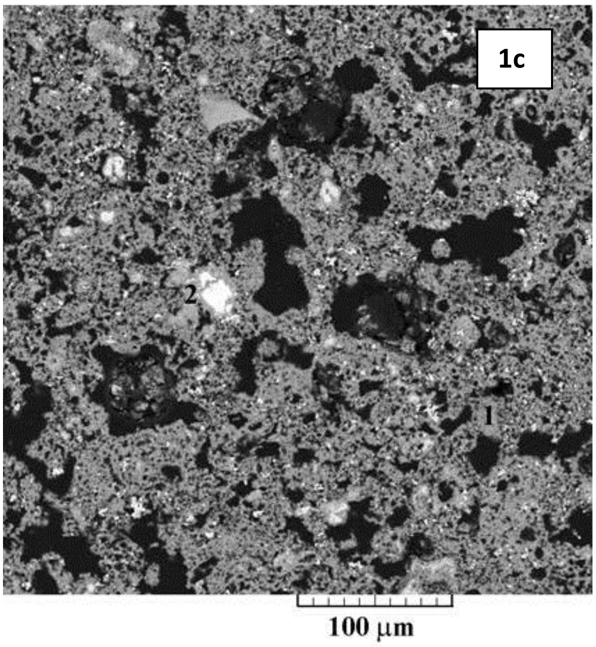

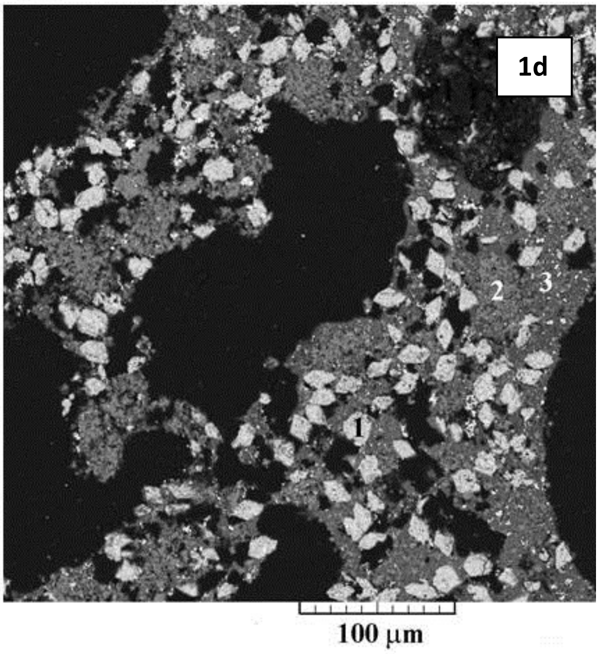

Fig. 1a. Zirsinalite (1) and parakeldyshite (2). Route 55. Imaging in backscattered electrons.
Fig. 1b. Parakeldyshite (1) and zirsinalite (2). Route 56. Imaging in backscattered electrons.
Fig. 1c. EGM (1) and aegirine-augite (2). Route 57. Imaging in backscattered electrons.
Fig. 1d. Parakeldyshite (1), zirsinalite (2), and EGM (3). Route 58. Imaging in backscattered electrons.

The infrared spectroscopic study was performed in accordance with the State Assignment theme, state record number AAAA-A19-119092390076-7, and the rest of the work was performed under State Assignment theme FMUF-2022-0002.

References

1. Christophe-Michel-Lévy M. Reproduction artificielle de quelques minéraux riches en zirconium (zircon, eudialyte, catapléite, elpidite); comparaison avec leurs conditions naturelles de formation, Bulletin de la Société française de Minéralogie et de Cristallographie. 1961. Vol. 84. № 3. P. 265–269. https://doi.org/10.3406/bulmi.1961.5487.
2. Johnsen O., Ferraris G., Gault R.A., Grice J.D., Kampf A.R., Pekov I.V. Nomenclature of eudialyte-group minerals. Canadian Mineralogist. 2003. Vol. 41. P. 785–794. https://doi.org/10.2113/gscanmin.41.3.785.
3. Kovalskaya T.N., Ermolaeva V.N., Chukanov N.V., Varlamov D.A., Kovalskiy G.A., Kalinin G.M., Chaychuk K.D. Synthetic phases of eudialyte composition // Experiment in geosciences. 2022. Vol. 28. № 1. P. 81-84.
4. Kovalskaya T.N., Ermolaeva V.N., Chukanov N.V., Varlamov D.A., Kovalskiy G.A., Zakharchenko E.S., Kalinin G.M., Chaichuk K.D. Synthesis of Fe-deficient eudialyte analogues: Relationships between the composition of the reaction system and crystal-chemical features of the products // Mineralogical

Magazine. 2023. https://doi.org/10.1180/mgm.2023.1 (doi: 10.1180/mgm.2023.1).

5. Kovalskaya T.N., Ermolaeva V.N., Chukanov N.V., Varlamov D.A., Kovalsky G.A., Kalinin G.M., Chaichuk K.D. Synthetic phases of eudialyte composition // Proceedings of the All-Russian Annual Symposium on Experimental Mineralogy, Petrology and Geochemistry (VESEMPG-2022). Moscow: GEOKHI RAS, 2022 P. 210-215.

Kovalskaya T.N.[1], Ermolaeva V.N.[1,2], Kovalskiy G.A.[1], Varlamov D.A.[1,3], Chukanov N.V.[3], Chaychuk K.D.[1] Synthesis of zircono- and titanosilicates under high alkalinity conditions

[1] – IEM RAS, Chernogolovka; [2] – GEOKHI RAS, Moscow; [3] – FRC PCP MC RAS, Chernogolovka
tatiana76@iem.ac.ru

Abstract. Synthesis of zircono- and titanosilicates in the presence of fluid of different alkalinity was carried out at 600 °C and 2 kbar. Such paragenesis is observed in postmagmatic formations of the Khibiny and Lovozero ultraagpaite complexes. The duration of the experiments was 10 days. The following mineral-like phases were diagnosed in the products of the experiments using electron-probe microanalysis and XRD: eudialyte group minerals, lovozerite group minerals, parakeldyshite.

Keywords: *synthesis, zirconosilicates, eudialyte, lovozerite, lovenite, postmagmatic processes, alkaline massifs, alkaline fluid.*

Alkaline massifs (Khibiny, Lovozero, Ilimaussaq) are characterized by a great variety of zircono- and titanosilicates. In particular, zirconosilicates of eudialyte and lovozerite groups, elpidite, parakeldyshite and some other minerals are typical components of some types of alkaline rocks and pegmatites, where they play the role of the main concentrators of zirconium; and lorenzenite, titanite, alluaivite and other minerals - concentrators of titanium. To obtain information on the conditions of their formation, as well as to study the influence of the fluid regime on the composition of the formed phases, a number of experiments on their synthesis were carried out.

Experiments on synthesis of zircono- and titanosilicates were carried out at temperature 600°C and pressure 2 kbar for 10 days under alkaline conditions. For the synthesis of zirconosilicates, the sol-gels prepared by the gel technique were used for the synthesis of lovenite composition $(Na,Ca)_2(Mn_{0.75}Fe^{2+}_{0.25})(Zr,Ti)Si_2O_7(O,OH,F)$ and $(Na,Ca)_2(Fe^{2+}_{0.75}Mn_{0.25})(Zr,Ti)Si_2O_7(O,OH,F)$. For the synthesis of titanosilicates, similar sol-gels of the alluaivite composition $Na_{19}(Ca_3Mn^{2+}_3)Ti_2NbSi_{26}O_{74}Cl{\cdot}2H_2O$ and $Na_{19}(Ca_3Mn^{2+}_{2.25}Fe^{2+}_{0.75})Ti_2NbSi_{26}O_{74}Cl{\cdot}2H_2O$ were used. During preparation, the required reactants were successively added to nitric acid solution, then the resulting solution was evaporated, coagulated with isopropyl alcohol and aqueous ammonia, and then calcined at 600°C and atmospheric pressure in a muffle furnace. A mixture (1:1) of 1M NaF solution with 5%, 10% or 20% NaOH solution was used as a fluid for the synthesis of zirconosilicates, 1M NaCl solution and a mixture (1:1) of 1M NaCl solution with 15% NaOH solution was used for the synthesis of titanosilicates. In one of the experiments on synthesis of titanosilicates the seed of eudialyte composition (2% of the weight of the suspension) was also added. The starting mixture and fluid were placed in ampoules, which were then welded and checked for tightness.

According to electron probe microanalysis data, synthesis of zirconosilicates using a mixture of 1M NaF with 5% NaOH resulted in the formation of parakeldyshite, lovenite (or its Fe-dominant analog), aegirine, and hematite (Fig. 1).

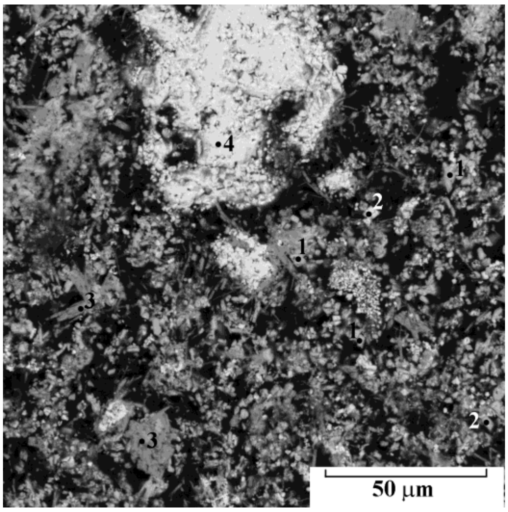

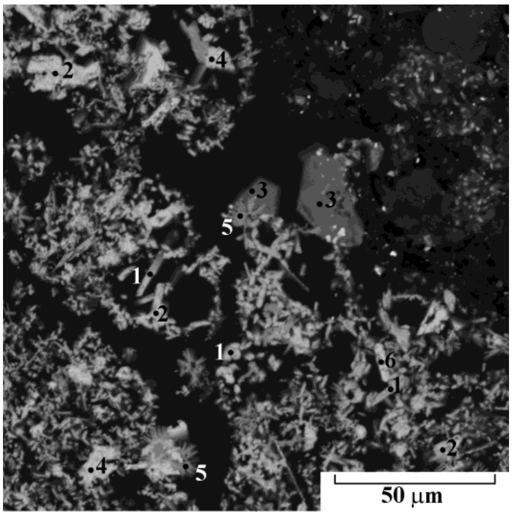

Fig. 1. 1 – parakeldyshite, 2 – Fe-dominant analog of lovenite, 3 – aegirine, 4 – hematite.
Fig. 2. 1 – parakeldyshite, 2 – lovenite, 3 – nepheline, 4 – tephroite, 5 – aegirine, 6 – pyrophanite.

When a mixture of 1M NaF with 10% NaOH was used, parakeldyshite, lovenite, burpalite, tephroite, aegirine, nepheline, zircon, pyrophanite, siderite, hematite, and quartz were formed (Figures 2,3). When a mixture of 1M NaF solution with 20% NaOH solution was added as a fluid, lueshite, F analog of lakargiite $CaZrF_6$, hematite, and quartz were formed (Fig. 4).

As a result of synthesis of titanosilicates with addition of 1M NaCl solution, titanite, lueshite, serandite, pectolite and lorenzenite were formed (Fig. 5). In the case with the addition of a mixture of 1M NaCl solution with 15% NaOH solution, lorenzenite, titanite and lueshite were formed (Fig. 6).

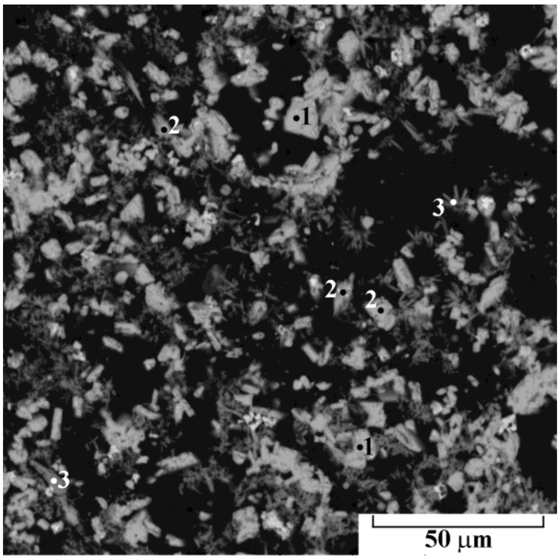

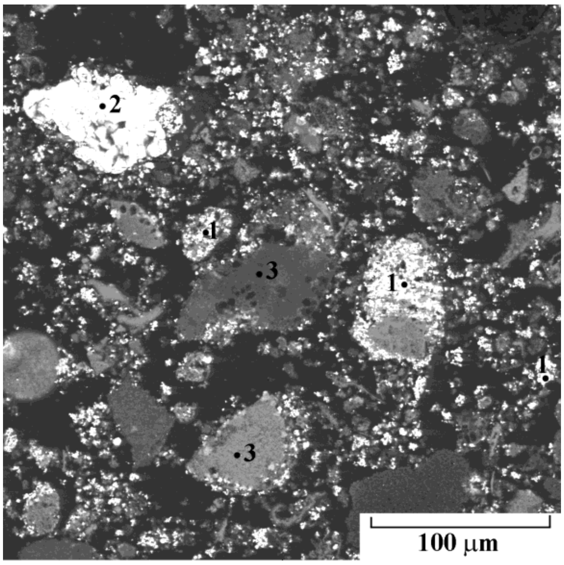

Fig. 3. 1 – parakeldyshite, 2 – burpalite, 3 – aegirine.
Fig. 4. 1 – lueshite, 2 – hematite, 3 – quartz.

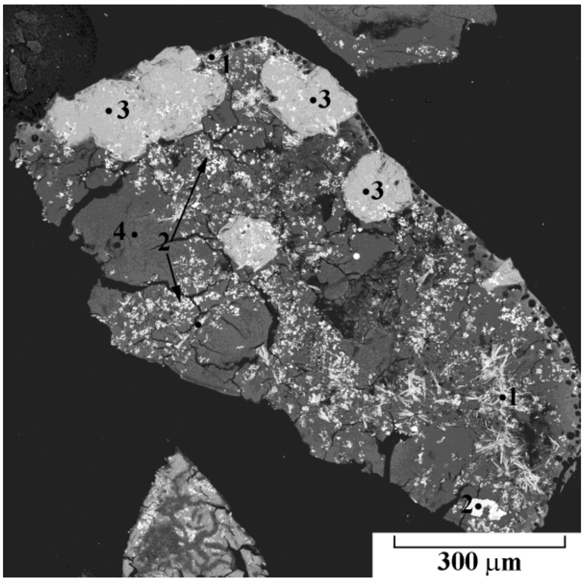

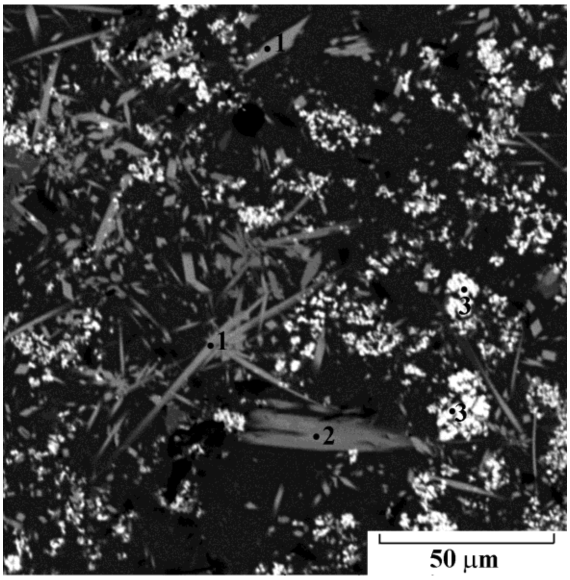

Fig. 5. 1 – titanite, 2 – lueshite, 3 – pectolite, 4 – serandite.
Fig. 6. 1 – titanite, 2 – lorenzenite, 3 – lueshite.

The results of the experiments show the influence of the fluid regime on the composition of crystallizing phases under the same conditions of temperature and pressure. In case of crystallization of zirconosilicates in less alkaline solution (1M NaF with 5-10% NaOH) the growth of zirconosilicates (parakeldyshite, lovenite and its Fe analog, burpalite, zircon) is observed, whereas in more alkaline solution (1M NaF with 20% NaOH) oxide lueshite and fluoride (F analog of lakargiite $CaZrF_6$) are formed. In the case of synthesis of titanosilicates, the addition of 15% NaOH solution to 1M NaCl solution does not significantly affect the crystallization of mineral phases (in both cases, the joint growth of lorenzenite, titanite and lueshite is observed).

The work was carried out within the framework of the IEM RAS research project FMUF-2022-0002, as well as at the expense of budgetary funding of the V.I. Vernadsky Institute of Geochemistry and Analytical Chemistry of the Russian Academy of Sciences (GEOCHI RAS).

References:

1. Kovalskaya T.N., Ermolaeva V.N., Chukanov N.V., Varlamov D.A., Kovalskiy G.A., Zakharchenko E.S., Kalinin G.M., Chaichuk K.D. Synthesis of Fe-deficient eudialyte analogues: Relationships between the composition of the reaction system and crystal-chemical features of the products // Mineralogical Magazine. 2023. Vol. 87. First View. P. 233 - 240. https://doi.org/10.1180/mgm.2023.1. DOI: 10.1180/mgm.2023.1.
2. Kovalskaya T.N., Ermolaeva V.N., Chukanov N.V., Kovalsky G.A., Varlamov D.A., Chaichuk K.D. Synthesis of zirconosilicates under conditions of high alkalinity // ZRMO. 2023. Ч. 152. № 4. С. 123-134. DOI: 10.31857/S0869605523040068.
3. Varlamov D.A., Kovalskaya T.N., Ermolaeva V.N., Chukanov N.V., Kovalsky G.A., Chaichuk K.D. Synthesis of mineral phases in the system Na_2O-CaO-FeO-Nb_2O_5-ZrO_2-SiO_2 under conditions of high alkalinity and application to natural processes // Collection of articles "Alkaline and kimberlite magmatism of the Earth and related strategic metal and diamonds deposits". Apatity: September 11-15, 2023. P. 43-46. DOI:10.37614/978-5-91137-500-3.008.

Redkin A.F. [1], **IonovA. M.** [2], **Nekrasov A.N.** [1], **Podobrazhnykh A.D.**[3], **Mozchil R.N.**[2]

Hydrothermal synthesis of platinum-antimony intermetallic compounds

[1] D.S. Korzhinskii Institute of Experimental Mineralogy RAS (IEM RAS), Chernogolovka, redkin@iem.ac.ru; [2] Institute of Solid State Physics RAS (ISSP RAS), Chernogolovka; [3] Lomonosov Moscow State University (MSU), Faculty of Geology, Moscow,

Abstract: Studies conducted in NaF-containing hydrothermal fluids have shown that the oxide compounds Sb^{5+} are unstable at 800°C, P_{total} = 200 MPa and fO_2 (fH_2) specified by Co-CoO and Ni-NiO buffers interact with the ampoule Pt material, forming antimony intermetallics with platinum on the inner surface of the ampoule. According to studies conducted on an electron microscope, the formation of the following intermetallics was established: $Pt_{90.3\pm0.8}Sb_{9.7}$ (~ $Pt_{10}Sb$), $Pt_{82.8\pm1.3}Sb_{17.2}$ (~ Pt_5Sb) and $Pt_{69.2\pm4.4}Sb_{30.8}$. The compound $Pt_{10}Sb$ obtained on the inner surface of the Pt ampoule is the limiting solid solution of antimony in platinum at 800°C, is of cubic structure of $Fm\bar{3}m$ (a=3.955(1) Å. The compound Pt_5Sb, presumably hexagonal $CaCu_5$ type structure $P6/mmm$ with unit cell parameters $a=b$=4.56(4), c=4.229(2) Å, α=β=90°, γ=120°, forms a thin film (≤ 10 μm) on the Pt surface and appears to be a metastable phase. The intermetallic compound $Pt_{69}Sb_{31}$ is a rapidly cooled melt of appropriate composition.

Keywords: *hydrothermal synthesis, roméite, antimony, platinum, intermetallic, sodium fluoride solution.*

During experiments on the solubility of roméite $(CaNa)Sb_2O_6F$ (Rom) at 800°C, P_{tot} = 200 MPa, under reducing conditions at $fO_2 \leq 10^{-3.47}$ Pa (Cu-Cu_2O buffer), it was found (Redkin et al., 2024; Redkin et al., 2024) that romeite is not stable, Sb^{5+} is reduced in solution and precipitates on the surface of the Pt ampoule is in the form of a compound of a composition close to Pt_5Sb. Analysis of literature data (Nemilov, Voronov, 1935; Hansen, 1936; Bhan et al., 1969; Kim, Chao, 1990; Duruselle, Feschotte, 1991; Kim, 1993; Okamoto, 1992; Itkin, Alcock, 1996; Liu et al., 2013) showed that at 500-900°C in the Pt-Sb system a number of compounds are formed ($PtSb_2$, PtSb, Pt_3Sb_2, Pt_5Sb_2, $Pt_{4+x}Sb$, Pt_5Sb, Pt_7Sb, Pt_xSb (fcc-face ceneter cubic)) and a Pt-Sb melt containing 27 -37 at.% Sb with eutectic at 630-690°C. Compounds of platinum and antimony, according to the definition, belong to the class of intermetallics, because. their crystal structure does not repeat the structures of their constituent metals (Pt and Sb). The phase diagrams in the Pt-Sb system of different authors are contradictory, which is associated with the methods of obtaining these compounds and the methods of their research. The works (Okamoto, 1992; Itkin, Alcock, 1996) analyzed the published data and constructed phase diagrams in the Pt-Sb system in the range 500-1800°C, which are identical to the diagram obtained experimentally (Duruselle, Feschotte, 1991). Since, according to these data, the stability of Pt_5Sb compound is limited to T=748±4°C, whereas we obtained this compound under hydrothermal conditions at 800°C, it was decided to investigate the possibility of synthesizing Pt_5Sb, including from other antimony oxide compounds.

The studies were carried out on a high-pressure hydrothermal installation in Pt ampoules measuring 5×0.2×50 mm in NaF solutions (4 and 10 wt.%). Redox conditions were set by copper-oxide, Ni-NiO and Co-CoO buffers. A mixture of CaO+NaF+Sb_2O_5, Sb_2O_5 reagents and fine-crystalline powder Pt+Sb_2O_5 were used as a charge. The duration of the experiments on the synthesis of Pt-Sb compounds was 24-48 hours.

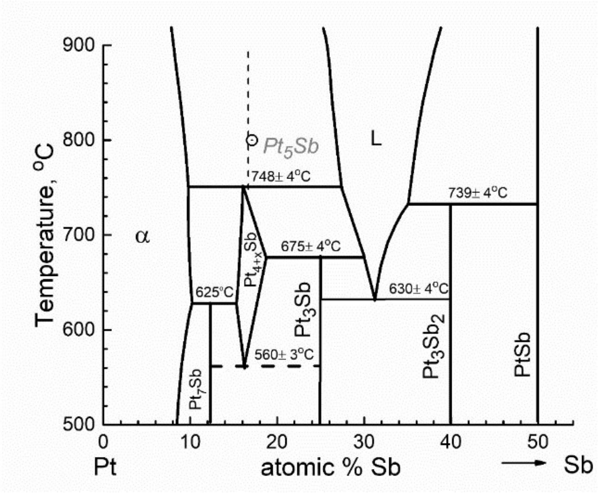

Fig. 1. Phase diagram in the Pt-Sb system according to data (Duruselle, Feschotte, 1991; Okamoto, 1992; Itkin, Alcock, 1996).

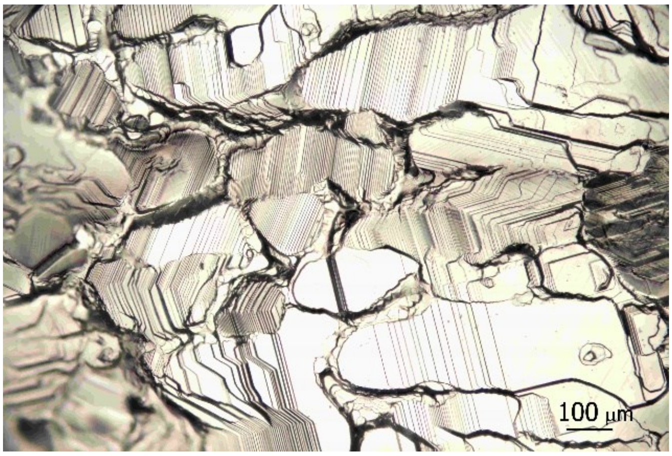

Fig. 2. Micrograph of a section of the inner surface of a Pt ampoule after experiments on the solubility of Rom in 4 wt.% NaF solution at 800°C, P_{tot} = 200 MPa and $fO_2 \leq 10^{-3.47}$ Pa.

We found that fine-crystalline Pt did not interact with Sb_2O_5 inside the ampoule, whereas the walls of platinum ampoules were altered to form lamellar crystals (Fig. 2) containing antimony. According to SEM analysis (64 measurements), the phase has a composition of $Pt_{82.8\pm1.3}Sb_{17.2\pm1.3}$, which corresponds to the formula $Pt_{4.82}Sb$ or Pt_5Sb. When analyzing the cross section of the lower part of the ampoule (Fig. 3), it was found that the antimony content in platinum varied from 18 ± 1 at.% (points 1-2) to 0 at.% (No. 20-22). According to the composition profile (Fig. 4), the inner layer of the ampoule up to 5-10 µm is represented by the Pt_5Sb compound, the middle layer from 10 to 45 µm is represented by the $Pt_{10}Sb$ compound and, finally, the outer part of the ampoule to a depth of 155 µm is pure Pt. Similar profiles were obtained in other experiments performed under Ni-NiO and Co-CoO buffer conditions, both using Sb_2O_5 and Rom as antimony containing agents. Increasing the duration of the experiments to 2 days increased the stability zone of the $Pt_{10}Sb$ (fcc) phase by approximately 2 times.

Of particular interest is the experiment where along with the charge composed of equimolar amounts of finely crystalline Pt and Sb_2O_5 (Pt:Sb=5:1), a seed plate cut from the 1-st experiment was introduced (Fig. 1-3). The experiment was carried out in a 10% solution of NaF and redox conditions specified by the Co-CoO buffer.

During the experiment, the Pt seed plate was welded to the wall of the Pt test tube. SEM analysis showed that the interaction of Pt ampoule with seed plate and antimony oxide at 800±2°C, 200±10 MPa, in a solution containing 10 wt.%. % NaF, fO_2 set by Co-CoO buffer ($fO_2 = 10^{-10.21}$ Pa), resulted in the formation of antimony solid solution (9.2 - 10.1 at.%) in platinum and the melt containing 30.8±4.4 at.% Sb and 69.2±4.4 at.% Pt. Single spheres of 70-150 µm in size were found inside the ampoule, representing quenched Pt-Sb melts. The composition of the balls is heterogeneous and is represented by two formations with a low content of antimony (11-12 at%) and containing high concentrations of Sb (27-28 at.%).

The inner surfaces of the ampoules were examined by XRD and XPS methods after the experiments. XRD analysis showed the presence of the following phases: Pt_5Sb - presumably of hexagonal structure of $CaCu_5$ $P6/mmm$ type with lattice constants a=b=4.56(4), c=4.229(2) Å, α=β=90°, γ=120°, $Pt_{10}Sb$ is of cubic $Fm\bar{3}m$ symmetry (LC: a = 3.955(1) Å) with a weakly developed surface <111> and Pt is of $Fm\bar{3}m$ having a =3.923(1) Å.

The study of electronic structure and valence states by XPS method on Kratos AXIS Ultra DLD electron spectrometer showed that Pt and Sb in Pt_5Sb and $Pt_{10}Sb$ compounds are in Pt^0 and Sb^0 states. The analysis of the valence band spectra shows the structure characteristic of metallic compounds with density of states in the range of 0-7 eV and appreciable intensity near the Fermi level, which indicates that these compounds belong to the class of intermetallics.

Studies have shown that the synthesis of Pt and Sb intermetallic compounds is observed in the zone most susceptible to hydrogen diffusion, i.e. on the walls of the Pt ampoule. The results of our research are most consistent with the data of [Kim, Chao, 1990; Kim, 1993]. The obtained Pt_5Sb phase containing 82.8±1.3 at.% Pt and 17.2±1.3 at.% Sb, presumably of hexagonal structure, appears to be metastable and at 800°C it should decompose into a fcc phase of composition $Pt_{9.2\pm0.7}Sb$ and a melt containing 26.4±0.9 at.% Sb and 73.6±0.9 at.% Pt. The formation of Pt_5Sb was observed only on the inner surface of Pt ampoules in a layer up to 10 µm thick.

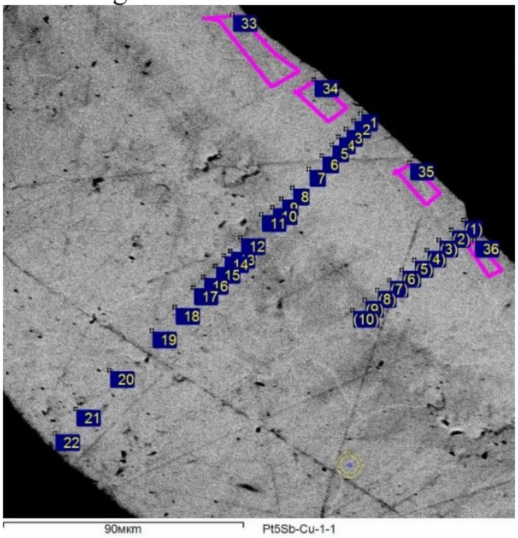

Fig. 3. The analyzed points (1-22, 1-10) and surfaces (33-36) of the cross section of the lower part of the ampoule, whose surface is shown in Fig. 2.

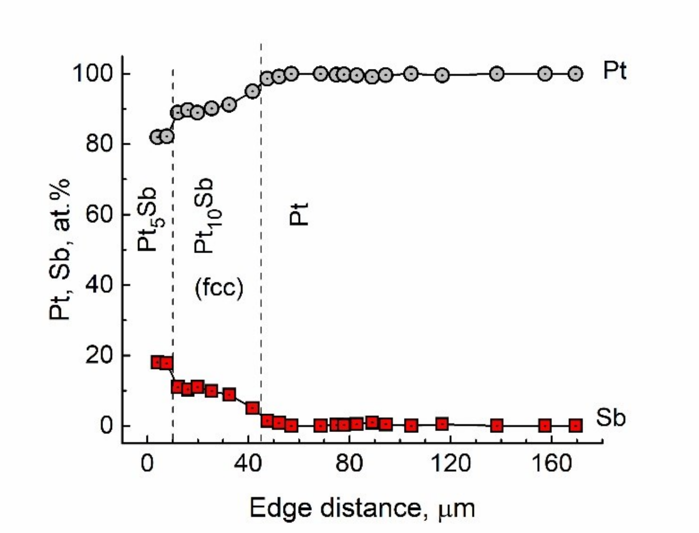

Fig. 4. The profile of the change in the composition of the Pt ampoule in an experiment on solubility of roméite at 800°C, P_{tot} = 200 MPa and $fO_2 \leq 10^{-3.47}$ Pa in a solution containing 1.0 mol·kg^{-1} (4.0 wt.%) NaF.

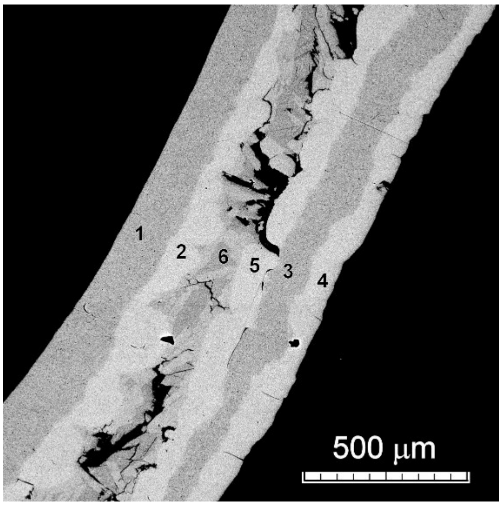

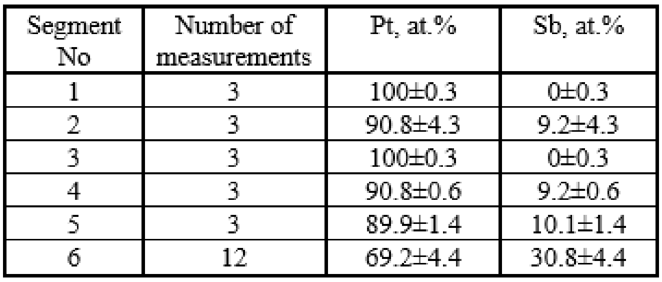

Segment No	Number of measurements	Pt, at.%	Sb, at.%
1	3	100±0.3	0±0.3
2	3	90.8±4.3	9.2±4.3
3	3	100±0.3	0±0.3
4	3	90.8±0.6	9.2±0.6
5	3	89.9±1.4	10.1±1.4
6	12	69.2±4.4	30.8±4.4

Fig. 5. The analyzed cross-sectional points of the ampoule with a seed. Co-CoO buffer, 10% NaF, a mixture of fine-grained Sb_2O_5 and Pt. SEM illustration captured using a BSE detector.

This work was supported by the Fundamental Research Program in the Russian Federation, projects FMUF-2022-0002, FMUF–2022-0003, and ISSP RAS state assignment.

References

1 Nemilow, W. A., & Woronow, N. M. (1936). Über Legierungen des Platins mit Antimon. Zeitschrift Für Anorganische Und Allgemeine Chemie, 226(2), 177–184.

2 Bhan S., Gödecke T., and Schubert K. (1969) Konstitution einiger mischungen des platins mit b-elementen (B = Sn, Sb, Te). J. Less-Common Met., 19(2), 121–140.

3 Durussel Ph., Feschotte P. (1991) Les Systèmes Binaires Pd-Sb et Pt-Sb. J. Alloy. Comp., 176 (1), 173-181.

4 Hansen, M. (1936). Der Aufbau der Zweistofflegierungen. Eine kritische Zusammenfassung. Springer-Verlag Berlin, Heidelberg. 1100 p.

5 Itkin, V.P., Alcock, C.B. The Pt-Sb (platinum-antimony) system. JPE 17, 356–361 (1996).

6 Kim W.-S., Chao G.Y. (1990). Phase relations in the system Pt-Sb-Te. Can. Mineral., 28, 675-685

7 Kim W.-S. (1993). Phase and phase equilibria in the Pt-Sb system. J. Korean Inst. Metals, 26 (3), 18-24.

8 Liu, J., Zhang, Y., Guo, C. (2013). Thermodynamic Assessment of the Pt-Sb System. International Journal of Nonferrous Metallurgy, 2, 95-99.

9 Okamoto, H. (1992). Pt-Sb (Platinum-Antimony). J. Phase Equilibria, 13(5), 580–581.

10 Redkin A.F., Kotova N.P., Shapovalov Yu.B., and Nekrasov A.N. Roméite solubility in the fluid immiscibility region of the NaF–H2O system at 800°C, 200 MPa. Geochem. *Inter.* 62 (4), 384–392.

Setkova T.V.[1], Vereshchagin O.S.[2], Spivak A.V.[1], Gorelova L.A.[2], Chistyakova D.A.[3] Growth of V-rich tourmaline on seed. *UDC: 549.612*

[1] Korzhinskii Institute of Experimental Mineralogy RAS; [2] Institute of Earth Sciences, St. Petersburg State University ; [3] Lomonosov Moscow State University;
setkova@iem.ac.ru

Abstract. In this work, for the first time, high vanadium tourmaline crystals were grown on elbaite seeds using the hydrothermal method of temperature difference at 600/650°C and 100 MPa in boric acid solutions. Phase diagnostics were performed using X-ray diffraction, electron probe microanalysis and Raman spectroscopy. The newly formed layer of dark green color of V-rich tourmaline towards the pinacoid direction reaches 700 µm thick. The distribution of vanadium in the overgrown layer is uniform ~14 wt. % V_2O_3 (~2 apfu). Synthetic analogs of jeremejevite and karelianite were diagnosed in the products of experiments together with V-rich tourmaline crystals.

***Keywords**: tourmaline, vanadium, hydrothermal synthesis, crystal growth, Raman spectroscopy.*

Tourmaline is a common borosilicate mineral with the general formula $XY_3Z_6T_6O_{18}(BO_3)_3V_3W$ (Henry et al. 2011), where X = Na^+, K^+, Ca^{2+}, vacancy; Y = Al^{3+}, Cr^{3+}, V^{3+}, $Fe^{2+/3+}$, Mg^{2+}, Mn^{2+}, Li^+, Ti^{4+}; Z = Al^{3+}, Cr^{3+}, V^{3+}, $Fe^{2+/3+}$, Mg^{2+}; T = Si^{4+}, Al^{3+}, B^{3+}; V = $(OH)^-$, O^{2-}; W = $(OH)^-$, F^-, O^{2-}. Tourmaline occurs in a wide range of geological settings, and differences in tourmaline chemistry make it a significant petrogenetic indicator of rock formation processes (Dutrow and Henry 2011). In addition to 41 mineral species (https://mineralogy-ima.org/Minlist.htm), more than 10 different compositions of synthetic tourmaline analogues have been obtained (Voskresenskaya et al., 1973; Setkova et al., 2019; Vereshchagin et al., 2020). However, the synthesis of tourmaline enriched with vanadium has not yet been carried out.

Tourmaline containing significant amounts of vanadium (4.41 – 32.03 wt.% V_2O_3) was found in metamorphic rocks of the Slyudyansky crystalline complex, Southern Baikal region (Reznitsky et al., 2001). So far, three minerals with species-determining vanadium have been identified in the tourmaline supergroup: oxy-vanadium-dravite, vanadium-oxy-dravite, vanadium-oxy-chrome-dravite (https://mineralogy-ima.org/Minlist.htm). The purpose of this study is the synthesis of tourmaline with a significant vanadium content.

The experiments were carried out in gold ampoules with a volume of 2 ml at a temperature of 600/650°C and a pressure of 100 MPa according to a previously developed method (Setkova et al. 2019).

The charge mixture was prepared from $V_2O_3/Al_2O_3/SiO_2$ oxides in a ratio of 1/4/4. The total weight of the solid oxide mixture was 1.8 g. In each experiment, an elbaite seed crystal was placed in the upper part of the ampoule to obtain large tourmaline crystals suitable for comprehensive study. Sodium and boron were in a solution based on deionized water with a concentration of 5 wt. % NaOH and 30 wt. % H_3BO_3. The amount of solution was set by the filling factor of the ampoule, which, according to PVT diagrams, corresponded to a pressure of 100 MPa. The ampoule was placed in a heat-resistant Cr-Ni alloy autoclave and heated to a specified temperature. The composition and morphology of the phases obtained in the experiments were studied at a scanning electron microscope (SEM) CamScanM2300 (VEGA TS 5130MM) with a Link INCA Energy-350 spectral analyzer (Table 1, Fig. 1). Raman spectroscopy was used to identify the V-rich tourmaline by comparing the Raman spectra of the natural seed with the newly formed layer. The spectra of the samples were recorded using a setup consisting of an Acton SpectraPro-2500i spectrograph with a Pixis2K CCD detector cooled to -70°C and an Olympus microscope with a continuous solid-state single-mode laser with a radiation wavelength of 532 nm. The laser beam was focused on the sample using an Olympus 50′objective to produce a spot with a of ~5 µm in diameter. The signal accumulation time was 540 s (3x180 s). The secondary phases obtained in the experiments were determined by X-ray analysis on a Bruker Advance 8 diffractometer.

As a result of the experiments, a growth on the seed of a dark green color up to 700 µm in size was obtained (Fig. 1a, b). An overgrown layer was formed on the faces of the pinacoid, both the <+0001> and <-0001> directions. The vanadium content in the overgrown layer is characterized by a uniform distribution and amounts to 13.60 wt.% V_2O_3, which corresponds to 2.03 *apfu* (Table 1). Numerous needle-shaped crystals of V-rich tourmaline (Fig. 1c, Table 1) up to 300 µm long were also found in the nutrient. They contain a small amount of nickel that got into the solution from the autoclave material. Other minor phases diagnosed by SEM and X-ray analysis are jeremeevite ($Al_6(BO_3)_5(F,OH)_3$) in the form of splices of needle-shaped crystals up to 200 µm and regular black crystals of karelianite (V_2O_3) about 50 µm in size (Fig. 1c ,d).

Table 1. Chemical composition of overgrown layer and spontaneous crystals of V-bearing tourmaline

Component	Overgrown layer	Spontaneous crystals
SiO_2	31.52	32.92
Al_2O_3	31.60	33.30
NiO	0.93	2.75
V_2O_3	13.60	10.92
Na_2O	0.65	0.50
Total	78.30	79.88

Apfu on 15 cations (*T*+*Y*+*Z*)			
Component		Overgrown layer	Spontaneous crystals
T	Si	5.88	5.94
	Al	0.12	0.06
	Total	**6**	**6**
Y+*Z*	Al	6.83	7.02
	V	2.03	1.58
	Ni	0.14	0.40
	Total	**9**	**9**
X	Na	0.24	0.17
	□	0.76	0.83
B	B	**3**	**3**
V+*W*	O	1.98	1.71
	OH	2.02	2.29

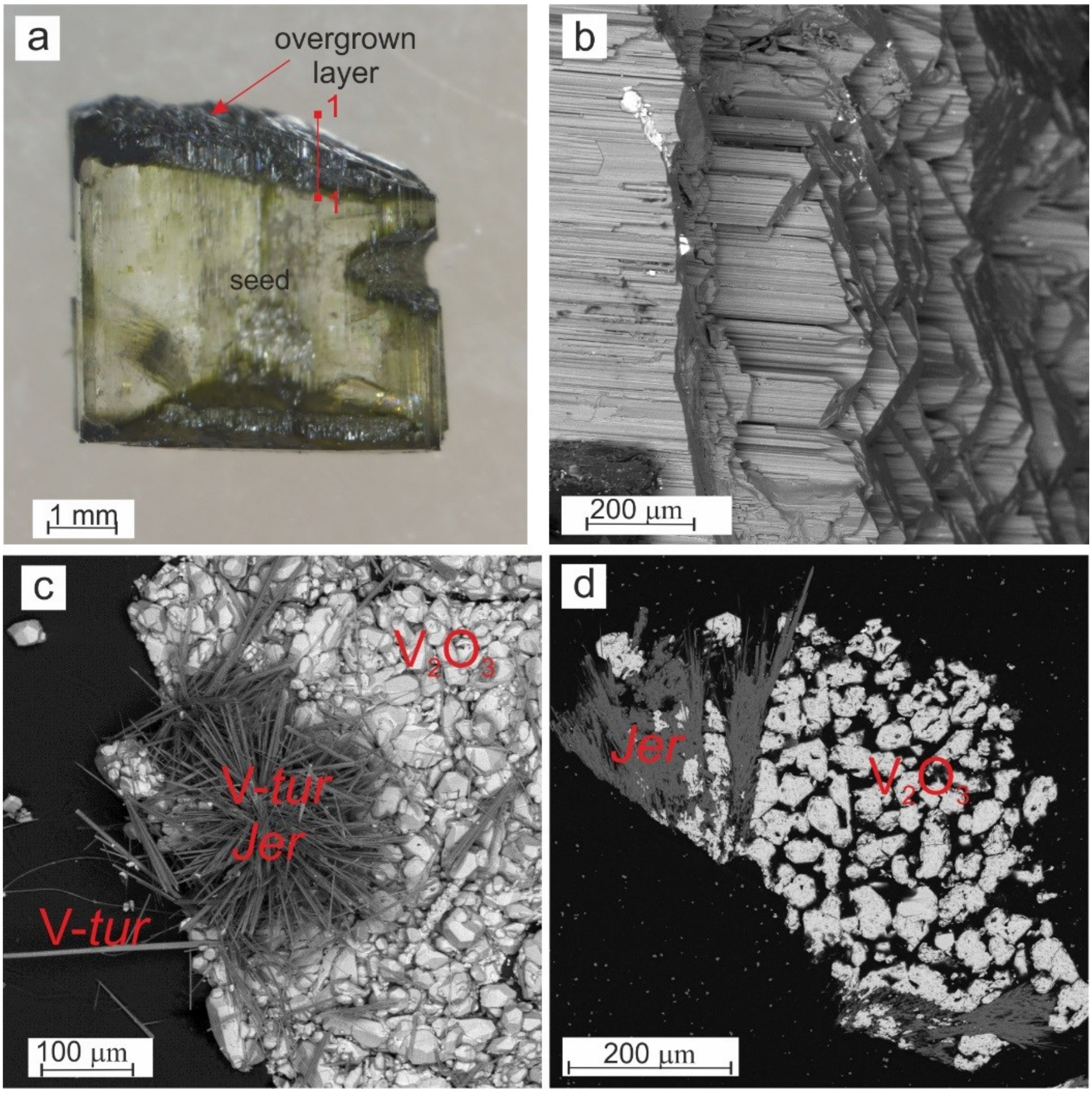

Fig. 1. (a) Growth of V-rich tourmaline on natural elbaite in <+0001> and <-0001> pinacoid directions; SEM images: (b) of the overgrown layer in the region of profile 1-1 labelled in Fig. 1a, (c) V-rich tourmaline of spontaneous nucleation and (d) secondary phases (Jer-jeremejevite and karelianite V_2O_3) diagnosed in the nutrient after experiments.

The Raman spectra of the natural seed and the grown layer of V-rich tourmaline were obtained in the range of 100-1400 cm-1 with bands of different intensities (Fig. 2). They have a similar topology. The shift in the main modes of the Raman spectrum of the synthetic V-rich tourmaline is observed. In the O-*Y*-O vibration region of ~220-230 cm^{-1} (Spivak at al., 2021), this shift is ~7 cm^{-1} towards higher frequencies for V-rich tourmaline, with the band at 311 cm^{-1} corresponding to the O – *Z* – O, Si – O(4.5) – Si and *Y*O6 vibrations of V-rich tourmaline becoming wider and more intense compared to the elbaite seed and shifting ~5 cm^{-1} towards lower frequencies.

The position of the intense band ~370 cm^{-1} (vibrations of the *Z*O6 octahedron) in the grown layer differs by ~4 cm^{-1} in the region of lower frequencies compared to the seed. Further, in the region of 400-600 cm^{-1}, corresponding to the Si-O-Si/O-B-O/B-O-Al vibrations, and in the region of the B-O vibrations of 600-800 cm^{-1}, a general slight shift towards the region of lower frequencies up to ~5 cm^{-1} was observed for the V-rich tourmaline compared to the seed.

Thus, for the first time, vanadium-rich tourmaline crystals have been grown on seeds using the hydrothermal temperature gradient method at 600/650°C and 100 MPa in boric acid solutions. The distribution of vanadium in the grown layer is uniform; its content is ~14 wt% V_2O_3. Crystals of V-rich tourmaline of spontaneous nucleation as well as synthetic analogues of jeremeevite and karelianite were diagnosed in the experimental products. A comparison of the Raman spectra of natural and synthetic tourmalines showed a shift of the main bands depending on the composition.

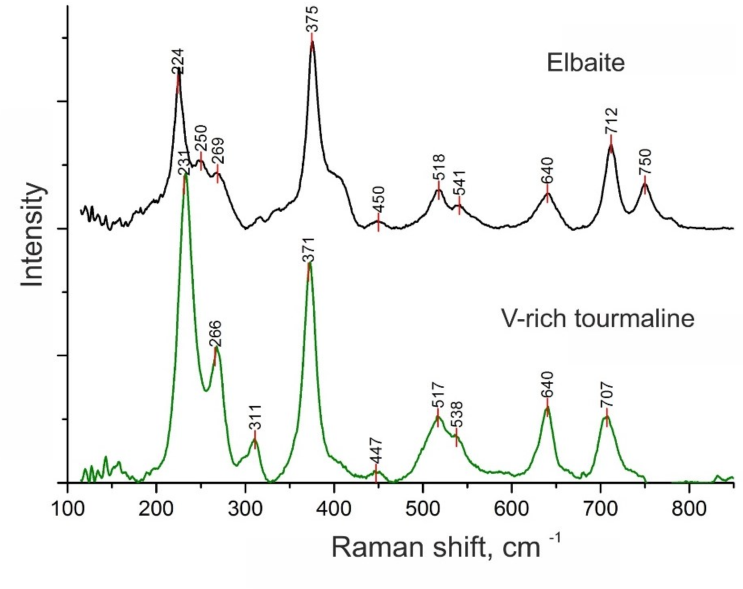

Fig. 2. Raman spectra of a natural elbaite seed and an overgrown layer of V-rich tourmaline.

This study is fulfilled under Research program № FMUF-2022-0002 of the Korzhinskii Institute of Experimental Mineralogy RAS.

References

Voskresenskaya I.E., Sternberg L.A. Synthesis of tourmaline in chloride media. Crystallography 1973, 19(4), 888-890. (in Russian).

Reznitsky L.Z. et al. Vanadium dravite $NaMg_3V_6[Si_6O_{18}][BO_3]_3(OH)_4$ is a new mineral from the tourmaline group. RMS Notes. 2001. No. 1. pp. 59-72. (in Russian).

Setkova, T. V., Balitsky, V. S., Shapovalov, Y. B. Experimental study of stability and synthesis of tourmaline group minerals. Geochemistry 64, 10, 2019, 1064-1078 (in Russian).

Dutrow, B.L., and Henry, D.J. Tourmaline: A geologic DVD. Elements, 2011, 7, 301–306.

Henry, D.J., Novák, M., Hawthorne, F.C., Ertl, A., Dutrow, B.L., Uher, P., and Pezzotta, F. Nomenclature of the tourmaline-supergroup minerals. American Mineralogist, 2011, 96, 895–913.

Spivak A.V., Borovikova E. Yu., Setkova T. V. Raman spectroscopy and high pressure study of synthetic Ga,Ge-rich tourmaline. Spectrochimica Acta - Part A: Molecular and Biomolecular Spectroscopy, 2021, 248:119171.

Vereshchagin, O.S.; Britvin, S. N.; Wunder, B.; Frank-Kamenetskaya, O.V.; Wilke, F. D. H.; Vlasenko, N. S.; Shilovskikh, V.V.; Bocharov, V. N.; Danilov, D. V. Ln^{3+} (Ln^{3+} = La, Nd, Eu, Yb) Incorporation in Synthetic Tourmaline Analogues: Towards Tourmaline REE Pattern Explanation. Chem. Geol. 2021, 584, 120526.